THE ASTROPHYSICAL JOURNAL, 982:192 (16pp), 2025 April 1 https://doi.org/10.3847/1538-4357/adb719

The Halo Occupation Distribution Modeling of X-Ray-selected Active Galactic Nuclei at $0.6 < z < 2.6$ in the COSMOS Field

Hiroyuki Ikeda[1], Takamitsu Miyaji[2], Taira Oogi[3], Yoshiki Toba[4,5,6,14], Héctor Aceves[2], Stefano Marchesi[7,8,9], Viola Allevato[10], Akke Viitanen[11,12], and Francesca Civano[13]

[1] National Institute of Technology, Wakayama College, Gobo, Wakayama 644-0023, Japan; ikedahr0@gmail.com
[2] Instituto de Astronomía, Universidad Nacional Autónoma de México, AP 106, Ensenada, Baja California, 22800, Mexico
[3] Department of Electrical and Computer Engineering, National Institute of Technology, Asahikawa College, Shunkodai 2-2-1-6, Asahikawa, Hokkaido 071-8142, Japan
[4] National Astronomical Observatory of Japan, 2-21-1 Osawa, Mitaka, Tokyo 181-8588, Japan
[5] Academia Sinica Institute of Astronomy and Astrophysics, 11F of Astronomy-Mathematics Building, AS/NTU, No.1, Section 4, Roosevelt Road, Taipei 10617, Taiwan
[6] Research Center for Space and Cosmic Evolution, Ehime University, 2-5 Bunkyo-cho, Matsuyama, Ehime 790-8577, Japan
[7] Dipartimento di Fisica e Astronomia (DIFA), Università di Bologna, via Gobetti 93/2, I-40129 Bologna, Italy
[8] Department of Physics and Astronomy, Clemson University, Kinard Lab of Physics, Clemson, SC 29634-0978, USA
[9] INAF—Osservatorio di Astrofisica e Scienza dello Spazio di Bologna, Via Piero Gobetti, 93/3, 40129, Bologna, Italy
[10] INAF—Osservatorio Astronomico di Capodimonte, Salita Moiariello 16, 80131, Napoli, Italy
[11] INAF—Osservatorio Astronomico di Roma, via Frascati 33, 00040 Monteporzio Catone, Italy
[12] Department of Physics, University of Helsinki, P.O. Box 64, FI-00014 Helsinki, Finland
[13] Astrophysics Science Division, NASA Goddard Space Flight Center, Greenbelt, MD 20771, USA

Received 2024 May 9; revised 2025 February 12; accepted 2025 February 15; published 2025 March 28

Abstract

We conduct precise measurements of active galactic nucleus (AGN) clustering at $z \sim 1$ and $z \sim 2$ by measuring the two-point cross-correlation function (CCF) between galaxies and X-ray-selected AGNs, and the two-point autocorrelation function (ACF) of galaxies in the COSMOS field, to interpret the CCF results. The galaxy sample was selected from the COSMOS2015 catalog, while the AGN sample was chosen from the Chandra-COSMOS Legacy Survey catalog. For the AGN samples at $z \sim 1$ and $z \sim 2$, we calculated AGN bias values of $b = 1.16$ (1.16; 1.31) and $b = 2.95$ (2.30; 3.55), respectively. These values correspond to typical host dark matter halo (DMH) masses of $\log(M_{\rm typ}/M_{\odot}) = 11.82$ (11.82; 12.12) and $\log(M_{\rm typ}/M_{\odot}) = 12.80$ (12.38; 13.06), respectively. Subsequently, we performed halo occupation distribution (HOD) modeling of X-ray-selected AGNs using the CCF and ACF of galaxies. We found a significant satellite AGN population at $z \sim 1$ all over the DMH mass ($M_{\rm DMH}$) range occupied by AGNs, while $z \sim 2$ AGNs in our sample are associated with higher-mass DMHs and smaller satellite fractions. The HOD analysis suggests a marginal tendency of increasing satellite slope with redshift, but larger samples are needed to confirm this with sufficient statistical significance. We find that the best-fit values of the satellite slope in both redshift bins are greater than 0, suggesting a tendency of increasing satellite AGN number with $M_{\rm DMH}$.

Unified Astronomy Thesaurus concepts: X-ray active galactic nuclei (2035); Active galactic nuclei (16)

1. Introduction

Previous observations have shown that a small fraction of galaxies exhibit active galactic nucleus (AGN) activity. It is well established that almost all galaxies have a central supermassive black hole (BH), implying that the galaxies have gone through at least one period of AGN activity, i.e., accretion of material onto the nucleus, in the past. The conditions in and mechanisms by which AGN activity occurs have been the subject of intensive research. Observational clues for tackling this problem include the luminosity function of AGNs and its evolution (Y. Ueda et al. 2003, 2014; G. Hasinger et al. 2005; S. M. Croom et al. 2009; H. Ikeda et al. 2011, 2012; J. Aird et al. 2015; N. Kashikawa et al. 2015; T. Miyaji et al. 2015; S. Fotopoulou et al. 2016; P. Ranalli et al. 2016; J. Yang et al. 2016; M. Akiyama et al. 2018; Y. Matsuoka et al. 2018, 2023; T. T. Ananna et al. 2019; M. Niida et al. 2020), BH demography, and AGN host galaxy properties. AGN clustering gives alternative clues. The clustering measurements of AGNs provide us with where AGNs are in the Universe. Therefore, the two-point autocorrelation function (ACF) of AGNs has been studied by many investigators (e.g., T. Miyaji et al. 2007; Y. Ueda et al. 2008; R. Gilli et al. 2009; S. Starikova et al. 2011; L. Koutoulidis et al. 2013; V. Allevato et al. 2014, 2019; Y. Toba et al. 2017; A. Viitanen et al. 2019; M. Krumpe et al. 2023), as the most common measure of clustering. They have calculated the large-scale bias and found that the typical host dark matter halo (DMH) mass ($M_{\rm typ}$) is $\sim 10^{12.5}$–$10^{13.0} M_{\odot}$.

When the number of AGNs with known spectroscopic redshift ($z_{\rm sp}$) is small, the two-point cross-correlation function (CCF) between galaxies and AGNs is often used (e.g., K. L. Adelberger & C. C. Steidel 2005; H. Francke et al. 2008; A. L. Coil et al. 2009; G. Mountrichas et al. 2009; Y. Shen et al. 2013; H. Ikeda et al. 2015; C. Garcìa-Vergara et al. 2017, 2019; W. He et al. 2018; C. Krishnan et al. 2020; Y. Shirasaki et al. 2020). The typical host DMH mass can be studied by the large-scale (>1–2 Mpc) bias determined by the ACF of AGNs or the CCF between AGNs and galaxies,

---

[14] NAOJ Fellow.

assuming the linear biasing scheme. One of the popular ways of interpreting the correlation function (CF) is the halo occupation distribution (HOD) analysis (e.g., J. A. Peacock & R. E. Smith 2000; U. Seljak 2000; A. Cooray & R. Sheth 2002), where the CF is modeled as the sum of one-halo (1-h) and two-halo (2-h) terms, representing the contributions of pairs that are within the same DMHs and across different DMHs, respectively. By the HOD analysis, one can obtain not only the "typical" DMH mass, but also constraints on how the objects are distributed among the DMHs as a function of the DMH mass ($M_{\rm DMH}$). The tool developed for the HOD analysis is also used to measure the bias parameter accurately, by applying it to the linear regime or applying it to all scales. This has often been useful to improve on the linear bias measurements, where previous studies used the power-law approximation of CFs. The linear regime of the CFs is the Fourier transform of the mass density linear power spectrum and not a power law. Thus, using the proper linear power spectrum included in the HOD tools is a large improvement over using the simple power-law model, even in the case where information from the 1-h term is not used, e.g., due to the lack of sufficient signal at small scales, as is often the case for AGN ACFs.

X-ray-selected AGN clustering studies have been made mainly through ACFs (T. Miyaji et al. 2007; Y. Ueda et al. 2008; R. Gilli et al. 2009; S. Starikova et al. 2011; L. Koutoulidis et al. 2013; V. Allevato et al. 2014, 2019; A. Viitanen et al. 2019). On the other hand, due to the small number of AGN samples, taking a cross-correlation approach with a much larger sample of galaxies would give AGN clustering measurements with better statistical accuracy (T. Miyaji et al. 2011; M. Krumpe et al. 2012, 2018). Also, the limited spatial resolution of X-ray images is less of a problem with the CCF approach than with the ACF approach, since we use the positions of the optical counterparts selected by, e.g., the likelihood ratio technique (M. Salvato et al. 2011; S. Marchesi et al. 2016; T. Miyaji et al. 2024) or a Bayesian-based statistics (e.g., M. Salvato et al. 2018), and measure separations to the galaxies. While the spatial resolution is less of a problem with Chandra, its point-spread function (PSF) degrades with off-axis angle rapidly and the sources detected at large off-axis angles still suffer from the spatial resolution problem. This is a problem with an HOD-type analysis—hampering the 1-h term measurements probed at small scales.

Motivated by the above situation, precise clustering measurements through CCF studies and their HOD modelings of X-ray-selected AGNs have been made. The HOD modeling of X-ray-selected AGNs has occurred up to $z \sim 1$ (T. Miyaji et al. 2011; M. Krumpe et al. 2012, 2018). T. Miyaji et al. (2011) performed HOD modeling of the CCF at $z < 1$ and found a satellite slope $\alpha_s < 1$ (see Equation (14)). At $z > 1$, the HOD modeling of the CCF has not yet been investigated; therefore, the small-scale clustering at $z > 1$ has not yet been studied. Motivated by the situation described above, we perform HOD modeling of the CCF of galaxies and X-ray-selected AGNs at $0.6 < z < 2.6$ in the COSMOS field to present a precise AGN clustering at $z \sim 1$ and ~ 2 in the Universe.

The outline of this paper is as follows. In Section 2, we describe the data that we use in this study and the selection criteria for galaxies and AGNs. In Section 3, we describe the methods for the clustering measurements. In Sections 4, 5, and 6, we give our results, discussion, and summary. In the Appendix, we explain a problem we have encountered with our covariance matrix and its remedy. Throughout this paper, we adopt a ΛCDM cosmology, with $\Omega_m = 0.3$, $\Omega_\Lambda = 0.7$, $\sigma_8(z = 0) = 0.8$, and a Hubble constant of $H_0 = 70\, h_{70}\,{\rm km\,s^{-1}\,Mpc^{-1}}$ for X-ray luminosities and stellar masses, while $H_0 = 100\, h\,{\rm km\,s^{-1}\,Mpc^{-1}}$ is used for distances, to aid in better comparison with previous works. The AB magnitude system is used (J. B. Oke 1974).

2. Data

2.1. Galaxy Sample at $0.6 < z < 2.6$

We construct volume-limited stellar-mass-selected samples of galaxies by utilizing the COSMOS2015 catalog (C. Laigle et al. 2016)[15] to calculate the ACF of galaxies and CCF of galaxies and X-ray-selected AGNs. This catalog has >30 band photometry and accurate photometric redshift ($z_{\rm ph}$) information over the 2 deg^2 of COSMOS. The photometric redshift precision is $\sigma_{\Delta z/(1+z_{\rm sp})} = 0.007$. The stellar-mass–redshift plane of galaxies is shown in the left panel of Figure 1. We try to make the galaxy sample as homogeneous and volume-limited as possible, to minimize the effects of redshift evolution within a redshift bin.

In order to construct volume-limited stellar-mass-selected samples of galaxies, we utilize two selection criteria, as follows:

$$9.5 < \log(M_*/M_\odot) < 10.0, \tag{1}$$

$$K_{AB} < 25.0, \tag{2}$$

where, M_* is the stellar mass of galaxies. In order to study the redshift evolution, we divide our galaxy sample in two bins of redshift. To construct a $z \sim 1$ galaxy sample, we add a selection criterion relating to the redshift of galaxies with known spectroscopic redshifts:

$$0.6 < z_{\rm sp} < 1.4. \tag{3}$$

We include objects without spectroscopic redshift measurements if they have photometric redshift measurements and non-negligible probabilities of being within this redshift range. Specifically, we include an object if its photometric redshift probability distribution function (PDFz(z)), provided by the COSMOS2015 catalog, satisfies

$$\text{PDFz}(0.6 < z_{\rm ph} < 1.4) > 0.025. \tag{4}$$

To construct a $z \sim 2$ galaxy sample, we add a selection criterion relating to the redshift of galaxies with known spectroscopic redshifts:

$$1.4 < z_{\rm sp} < 2.6. \tag{5}$$

For those without known spectroscopic redshifts but with photometric redshift measurements, we include those that satisfy

$$\text{PDFz}(1.4 < z_{\rm ph} < 2.6) > 0.025. \tag{6}$$

Using Equations (1)–(6), we construct $z \sim 1$ and $z \sim 2$ stellar-mass-selected galaxy samples. These galaxy samples are listed in Table 1, and the spatial and redshift distributions of these samples are shown in Figure 2.

---

[15] Recently, the COSMOS2020 catalog (J. R. Weaver et al. 2022) has become public. Most of the work in this paper was done before the publication of the COSMOS2020 catalog.

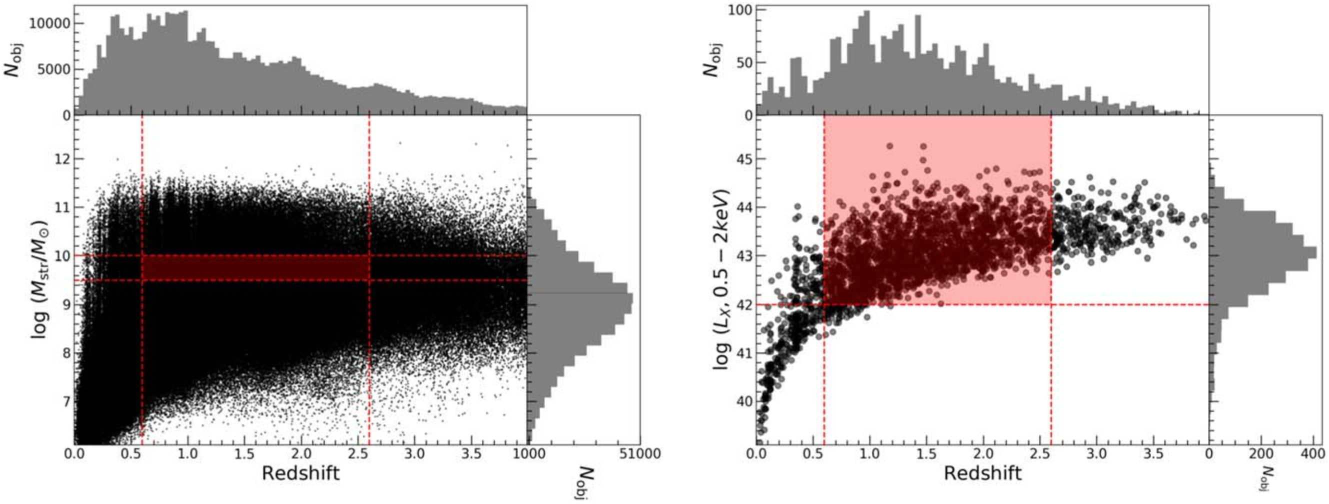

Figure 1. Left: distribution of stellar mass as a function of redshift for galaxies at $0 < z < 4$ in the COSMOS2015 catalog. The red shaded region denotes the selection criteria for our sample. Right: distribution of 0.5–2 keV X-ray luminosity as a function of redshift for Chandra legacy X-ray-selected AGNs at $0 < z < 4$. The red shaded region denotes the selection criteria for our sample.

Table 1
Properties of Galaxy Samples

Sample Name	Redshift Range	$\log M_*$ Range ($h^{-1}\,M_\odot$)	Number	$\langle n_{\rm gal}\rangle$ (h^3 Mpc^{-3})	$\langle z_{\rm med}\rangle$	$\langle \log M_*\rangle$ ($h^{-1}\,M_\odot$)
$z \sim 1$ galaxy sample	$0.6 < z < 1.4$	$9.5 < \log(M_*/M_\odot) < 10.0$	22,281	8.40×10^{-3}	1.01	9.72
$z \sim 2$ galaxy sample	$1.4 < z < 2.6$	$9.5 < \log(M_*/M_\odot) < 10.0$	18,874	3.22×10^{-3}	1.75	9.73

2.2. X-Ray-selected AGN Sample at $0.6 < z < 2.6$

We construct an X-ray-selected AGN sample by utilizing the Chandra Legacy Identification Catalog (S. Marchesi et al. 2016) to calculate the CCF of galaxies and X-ray-selected AGNs. This catalog contains the optical and infrared counterparts of the X-ray sources for the X-ray sources detected in the Chandra-COSMOS Legacy Survey (F. Civano et al. 2016). This catalog also includes information about the spectroscopic and photometric redshift. The photometric redshifts in S. Marchesi et al. (2016) are derived independently from those in C. Laigle et al. (2016) and optimized for X-ray-selected AGNs following M. Salvato et al. (2011). Those with photometric redshifts only are included in the sample in the same way as the galaxy sample using the PDFzs (denoted as "PDzs" in S. Marchesi et al. 2016). We consider X-ray sources that have $L_{\rm X} > 10^{42}\,h_{70}^{-2}$ erg s^{-1} (0.5–2 keV) as secure AGNs and include them in our sample. Given the limited number of X-ray-selected AGNs, constructing a volume-limited sample of AGNs is not feasible, and thus our AGN sample is essentially flux-limited. The $\log L_{\rm X}$(0.5–2 keV)–redshift plane of the X-ray-selected AGNs is shown in the right panel of Figure 1.

We choose the $z \sim 1$ and $z \sim 2$ X-ray-selected AGN samples in the same way as the corresponding galaxy samples, following Equations (3)–(6).

These samples are listed in Table 2, and the spatial and redshift distributions of these samples are shown in Figure 2.

3. Methods

3.1. ACF of Galaxies

In order to calculate the ACFs of galaxies, we use the S. D. Landy & A. S. Szalay (1993) estimator, in a two-dimensional grid in $(r_{\rm p}, \pi)$ space, where $r_{\rm p}$ is the projected distance and π is the line-of-sight separation:

$$\xi_{\rm ACF}(r_{\rm p}, \pi) = \frac{DD(r_{\rm p}, \pi) - 2DR(r_{\rm p}, \pi) + RR(r_{\rm p}, \pi)}{RR(r_{\rm p}, \pi)}, \quad (7)$$

where, DD, DR, and RR are the normalized number of pairs (see, e.g., Equation (3) of T. Miyaji et al. 2007) within the real sample, the number of pairs between the real sample and the random sample, and the number of pairs within the random sample, respectively. The random sample is created with 100 times the number of our galaxy samples, to match the redshift distribution of our galaxy sample. When an object has a photometric redshift only, it is included as if it were multiple objects at the same sky position with different redshifts, weighted by its PDFz(z) within the redshift range of interest, following the approach of V. Allevato et al. (2016).

We then calculate the projected CF:

$$w_{\rm p,ACF}(r_{\rm p}) = 2\int_0^{\pi_{\rm max}} \xi_{\rm ACF}(r_{\rm p}, \pi)d\pi, \quad (8)$$

where $\pi_{\rm max}$ is determined by the saturation of the integral. We calculate the errors of the ACF by using the jackknife resampling technique. The error and covariance matrix estimations are explained in Section 3.3. The saturating $\pi_{\rm max}$ value is found by plotting the projected galaxy ACF values in three large $r_{\rm p}$ bins as a function of $\pi_{\rm max}$. The upper panels of Figure 3 show that the amplitude of the projected galaxy ACF saturates at $\pi_{\rm max} \sim 190\,h^{-1}$ Mpc for $0.6 < z < 1.4$ and at $\pi_{\rm max} \sim 240\,h^{-1}$ Mpc for $1.4 < z < 2.6$, respectively. Thus, we adopt these $\pi_{\rm max}$ values for the ACFs for our subsequent analysis.

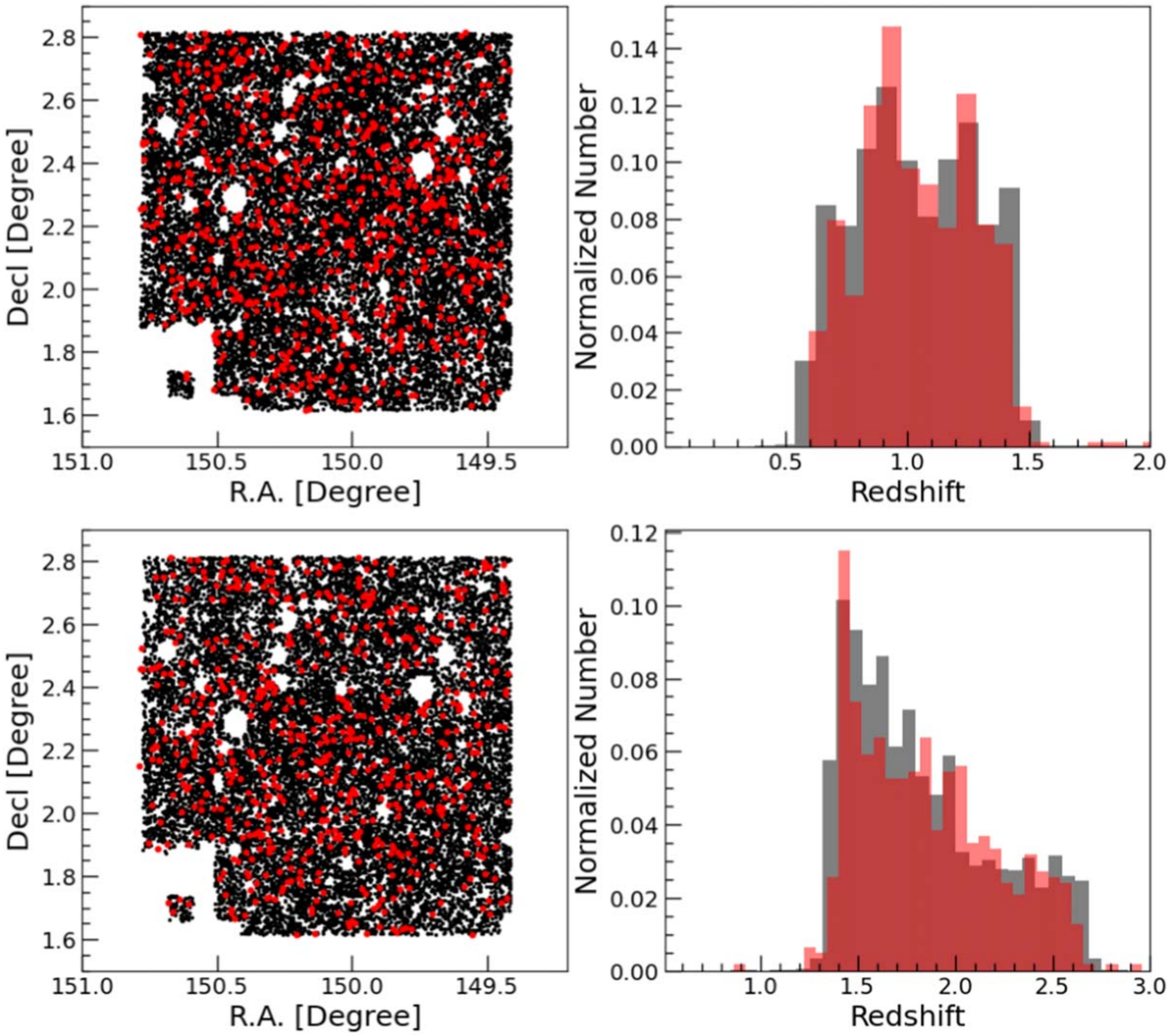

Figure 2. Upper left: the spatial distributions of the X-ray-selected AGNs and galaxies for the $0.6 < z < 1.4$ samples. The red and black circles represent X-ray-selected AGNs and galaxies, respectively. Upper right: the redshift distributions of the X-ray-selected AGNs and galaxies for the $0.6 < z < 1.4$ samples. The red and black histograms represent the X-ray-selected AGN and galaxy samples, respectively. Lower: the same as the upper panels but for the X-ray-selected AGNs and galaxies in the $1.4 < z < 2.6$ samples.

Table 2
Properties of X-Ray-selected AGN Samples

Sample Name	Redshift Range	$\log L_X$ Range (h_{70}^{-2} erg s^{-1})	Number	$\langle n_{\rm AGN} \rangle$ (h^3 Mpc^{-3})	$\langle z_{\rm med} \rangle$	$\langle \log L_X \rangle$ (h_{70}^{-2} erg s^{-1})
$z \sim 1$ X-ray-selected AGN sample	$0.6 < z < 1.4$	$\log L_X > 42$	718	2.71×10^{-4}	1.02	42.71
$z \sim 2$ X-ray-selected AGN sample	$1.4 < z < 2.6$	$\log L_X > 42$	626	1.23×10^{-4}	1.80	43.2

3.2. CCF Between Galaxies and AGNs

To calculate the CCFs of galaxies and AGNs, we use the S. D. Landy & A. S. Szalay (1993) estimator, which is modified for the CCF (K. L. Adelberger et al. 2003; N. Kashikawa et al. 2007; E. J. Bradshaw et al. 2011):

$$\xi_{\rm CCF}(r_{\rm p}, \pi) = \frac{D_{\rm G}D_{\rm A} - D_{\rm G}R_{\rm A} - R_{\rm G}D_{\rm A} + R_{\rm G}R_{\rm A}}{R_{\rm G}R_{\rm A}}, \qquad (9)$$

where $D_{\rm G}D_{\rm A}$, $D_{\rm G}R_{\rm A}$, $R_{\rm G}D_{\rm A}$, and $R_{\rm G}R_{\rm A}$ are the normalized numbers of the galaxy–AGN, galaxy–randomized AGN, randomized galaxy–AGN, and randomized galaxy–randomized AGN pairs falling into the given $(r_{\rm p}, \pi)$ bin, respectively. The random sample for galaxies and AGNs is created with 100 times the number of our galaxy and AGN sample, to match their redshift distribution. The PDFzs of the photometric redshifts in the galaxy and AGN samples are treated in the same way as the galaxy ACF case.

We then calculate the projected CF:

$$w_{\rm p,CCF}(r_{\rm p}) = 2\int_0^{\pi_{\rm max}} \xi_{\rm CCF}(r_{\rm p}, \pi)d\pi, \qquad (10)$$

where $\pi_{\rm max}$ is determined by the saturation of the integral. The lower panels of Figure 3 show $w_{\rm p}$ estimates for the CCF in three $r_{\rm p}$ bins as functions of $\pi_{\rm max}$, in the same way as the ACF. From this figure, we observe that the projected CCF estimates saturate at $\pi_{\rm max} \sim 200\,h^{-1}$ Mpc for $0.6 < z < 1.4$ and at

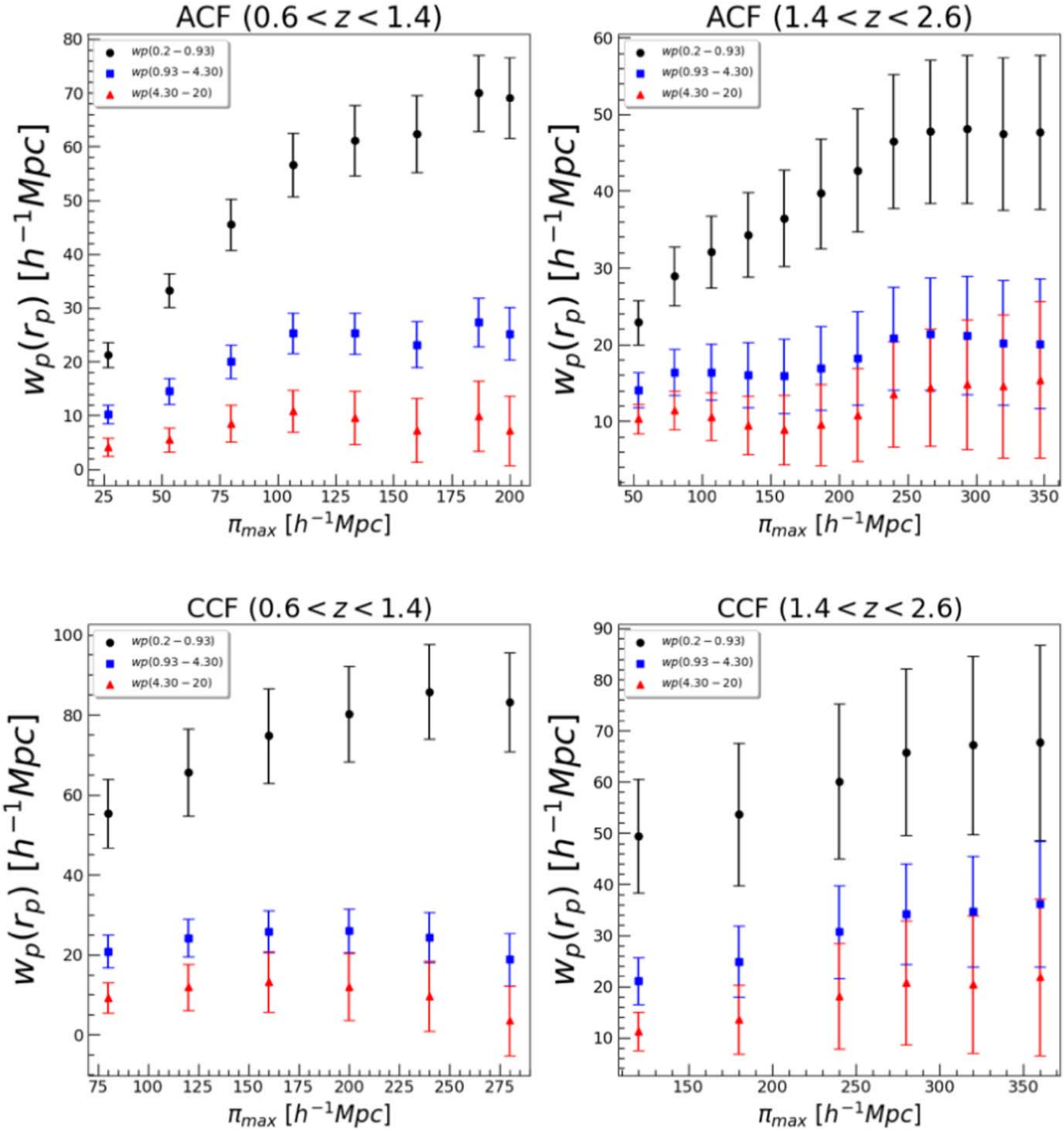

Figure 3. Upper: the ACFs of galaxies at $0.6 < z < 1.4$ (left) and $1.4 < z < 2.6$ (right) as a function of $\pi_{\rm max}$ [h^{-1}Mpc]. The black circles, blue squares, and red triangles are the ACFs at $0.2 < r_{\rm p}$ [h^{-1} Mpc] < 0.93, $0.93 < r_{\rm p}$ [h^{-1} Mpc] < 4.30, and $4.30 < r_{\rm p}$ [h^{-1} Mpc] < 20.0, respectively. Lower: same as the upper panels but for the CCFs of galaxies and AGNs.

$\pi_{\rm max} \sim 300\,h^{-1}$ Mpc for $1.4 < z < 2.6$, respectively. We adopt these $\pi_{\rm max}$ values for the CCFs for our subsequent analysis.

3.3. Errors and Covariance Matrix

We calculate the errors of ACF and CCF by using the jackknife resampling technique. We divide the survey area into $N = 16$ (4×4) subsections. The kth $(k = 1..N)$ jackknifed sample is constructed by excluding the objects (both from the real and random samples) in the kth subsection and $w_{{\rm p}ik}$ is the ACF or CCF, depending on the i value, calculated from the kth jackknifed sample. The index i runs through $r_{\rm p}$ bins of the ACF followed by those of the CCF. The N jackknife-resampled CFs define the covariance matrix, M_{ij}:

$$M_{ij} = \frac{N-1}{N}\sum_{k=1}^{N}[w_{{\rm p}ik}(r_{{\rm p},i}) - \langle w_{{\rm p}i}(r_{{\rm p},i})\rangle] \times [w_{{\rm p}jk}(r_{{\rm p},j}) - \langle w_{{\rm p}j}(r_{\rm p,j})\rangle]. \tag{11}$$

The 1σ error bar for the ith bin corresponds to $\sqrt{M_{ii}}$. In constructing the covariance matrix, we initially considered not only the errors in different $r_{\rm p}$ bins within each of the ACF and CCF but also those across the ACF and CCF to be correlated. However, due to the inaccuracies of the off-diagonal elements, especially those across the ACF/CCF, we only use the off-diagonal elements within the CCF, as explained in the Appendix.

3.4. The HOD Modeling

We perform the HOD modeling following an approach similar to T. Miyaji et al. (2011). We model the two-point projected CF as the sum of two terms:

$$w_{\rm p}(r_{\rm p}) = w_{\rm p,1h}(r_{\rm p}) + w_{\rm p,2h}(r_{\rm p}), \tag{12}$$

where $w_{\rm p,1h}(r_{\rm p})$ and $w_{\rm p,2h}(r_{\rm p})$ are the 1-h term contributed by pairs, where both the objects occupy the same DMH, and the 2-h term contributed by pairs, where the two objects occupy different DMHs, respectively. We use the halo mass function of R. K. Sheth et al. (2001) and the Navarro–Frenk–White DMH profile (J. F. Navarro et al. 1997) for the DMH density distribution in our HOD modeling. By performing a correlated χ^2 fit to both the ACF of galaxies and the galaxy–AGN CCF jointly, we can constrain the HOD of X-ray-selected AGNs.

Note that there have been several improvements and modifications of our HOD code after T. Miyaji et al. (2011). The scale-dependent bias and effects of halo–halo collision formulated by J. L. Tinker et al. (2005) have been included since the version of the code used in M. Krumpe et al. (2018). The Markov Chain Monte Carlo (MCMC) method for the HOD parameter search has also been included and used in M. Krumpe et al. (2023), where a two-step process was taken. In the first step, the galaxy HOD was determined from the galaxy ACF, and in the second step, the AGN HOD was determined from the galaxy–AGN CCF, assuming the fixed best-fit galaxy HOD parameters obtained in the first step, with separate MCMC chains. In this work, we search for HOD parameters and confidence ranges for the galaxies and AGNs by means of a simultaneous MCMC parameter search over the galaxy ACF and galaxy–AGN CCF.

3.4.1. The Parameterized HOD Model of Galaxies

One of the most common forms of the galaxy HOD is the combination of a step function with a smooth transition for the galaxies at halo centers and a power-law form multiplied by the central HOD, as proposed by Z. Zheng et al. (2005). This form is intended for luminosity-thresholding samples of galaxies, where it is assumed that the centers of most massive halos are always occupied by a galaxy in the sample. Since our galaxy sample is not a luminosity-thresholding sample, the central HOD at the highest-halo-mass end does not have to saturate at unity. Since the HOD-predicted CF does not depend on the absolute normalization of the HOD, we express the central HOD with proportionality rather than equality. In comparing the HOD-model-predicted CF with the observed one, we also do not give the density constraint, since such a constraint is meaningful when the central HOD saturates at unity, which is not the case for our sample. Thus, our galaxy HOD has the form (Z. Zheng et al. 2007)

$$\langle N_{\rm G,c}\rangle(M_{\rm DMH}) \propto \frac{1}{2}\left[1+{\rm erf}\left(\frac{\log M_{\rm DMH}-\log M_{\rm min}}{\sigma_{\log M}}\right)\right] \tag{13}$$

for the centrals and the following form for the satellites:

$$\langle N_{\rm G,s}\rangle(M_{\rm DMH}) = \langle N_{\rm G,c}\rangle(M_{\rm DMH})\left(\frac{M_{\rm DMH}}{M_1}\right)^{\alpha_{\rm s}}, \tag{14}$$

where $M_{\rm min}$, $\sigma_{\log M}$, and M_1 are the characteristic minimum mass of halos that can host central galaxies, the width of the cutoff profile, and the normalization of the satellite HOD, respectively.

3.4.2. The Parameterized HOD Model of X-Ray-selected AGNs

In our HOD model of X-ray-selected AGNs, we use the occupation function for central AGNs as follows:

$$\langle N_{\rm A,c}\rangle = f_{\rm A}\,\Theta(M_{\rm DMH} - M_{\rm min}), \tag{15}$$

while the occupation function for satellite AGNs is expressed as follows:

$$\langle N_{\rm A,s}\rangle = f_{\rm A}\,\Theta(M_{\rm DMH} - M_{\rm min})(M_{\rm DMH}/M_1)^{\alpha_{\rm s}}, \tag{16}$$

where $f_{\rm A}$ is the AGN fraction among central galaxies at $M_{\rm DMH} \gtrsim M_{\rm min}$ and $\Theta(x)$ is a step function that has the value of 0 at $x < 0$ and 1 at $x \geqslant 0$, respectively. We do not introduce the smoothing of the step function through the parameter $\sigma_{\log M}$ for the AGN HOD, because this parameter is found to be poorly constrained and pegged at zero when it is made a free parameter. Again, we fix M_0 to 0. The HOD has implications for the AGN population that are satellites. The satellite fraction $f_{\rm sat}$ is often calculated in the literature from the AGN HOD analysis. The satellite fraction can be calculated by

$$f_{\rm sat} = \frac{\int \langle N_{\rm A,s}\rangle(d\phi/d\log M_{\rm DMH})d\log M_{\rm DMH}}{\int(\langle N_{\rm A,c}\rangle + \langle N_{\rm A,s}\rangle)(d\phi/d\log M_{\rm DMH})d\log M_{\rm DMH}}, \tag{17}$$

where $d\phi/d\log M_{\rm DMH}$ is the halo mass function. We note that this satellite fraction depends on the form of the HOD model and should not be interpreted literally. Because of the rapidly dropping nature of the DMH mass function, $f_{\rm sat}$ is dominantly contributed by the satellite population at the low-DMH-mass end, near $M_{\rm min}$. We calculate the satellite fraction as a rough indicator of the importance of satellites among the AGN population in $M_{\rm DMH} \sim M_{\rm min}$ halos and a comparison between the satellite populations in the $z \sim 1$ and $z \sim 2$ samples.

3.5. The χ^2 Minimization

To find the galaxy and AGN HODs from the galaxy ACF and galaxy–AGN CCF, we minimize the joint χ^2 to the ACF and CCF. Unlike the case of, e.g., T. Miyaji et al. (2011), the errors on the galaxy HOD parameters from the ACF are not negligible. Thus, we choose not to fix the galaxy HOD parameters to search for confidence ranges of the AGN HOD parameters, but we fit the galaxy ACF and galaxy–AGN CCF

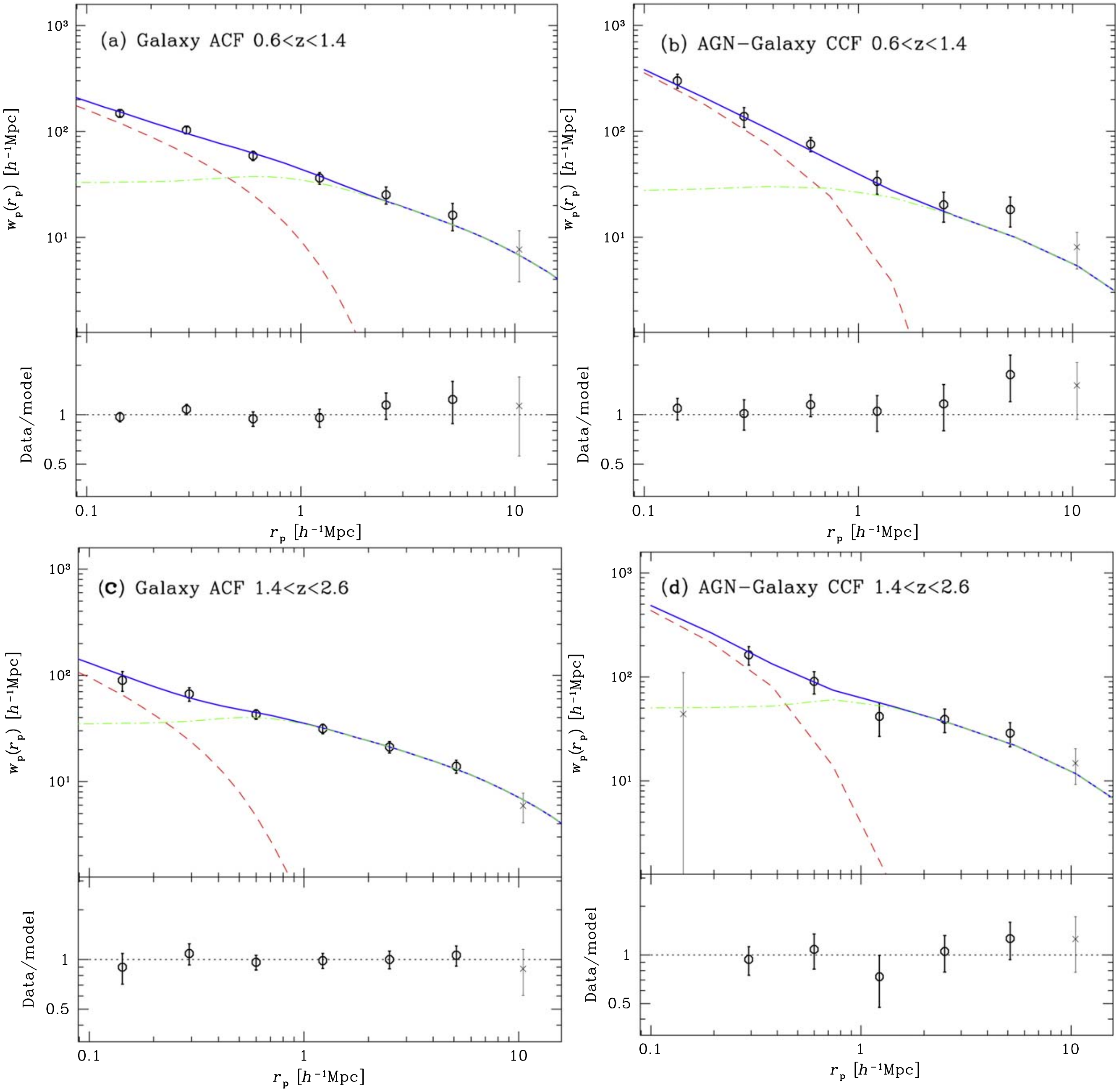

Figure 4. Upper left: the ACF of galaxies at $0.6 < z < 1.4$, and the best-fit HOD model with residuals. The data points and error bars show our measurements of the galaxy ACF. The circles show the data points that are used for the fit, while the crosses show those excluded. The short dashed (red), long dashed (green), and solid (blue) lines show the 1-h term, the 2-h term, and the total, respectively. Upper right: same as upper left but for the CCF of galaxies and AGNs at $0.6 < z < 1.4$. Lower left: same as upper left but for the ACF of galaxies at $1.4 < z < 2.6$. Lower right: same as upper left but for the CCF of galaxies and AGNs at $1.4 < z < 2.6$.

simultaneously by minimizing

$$\chi^2 = \sum_{i,j} [(w_{\mathrm{p}i}(r_{\mathrm{p},i}) - w_{\mathrm{p,mdl}i}(r_{\mathrm{p},i})] M_{ij}^{-1} [w_{\mathrm{p}j}(r_{\mathrm{p},j}) - w_{\mathrm{p,mdl}j}(r_{\mathrm{p},j})]. \tag{18}$$

See Section 3.3 for the indices i and j. The subscript "mdl" means the model value evaluated at the center of the bin. As explained in the Appendix, for our final results, we use all the diagonal elements of M_{ij} and its off-diagonal elements within the CCF only, while neglecting other off-diagonal elements. Note that the ACF model depends on the galaxy HOD parameters only, while the CCF model depends on both the galaxy and AGN HOD parameters.

he χ^2 minimizations and determinations of the HOD parameters for the confidence ranges are made with an MCMC method using the MCMC-F90 library by Marko Laine,[16] modified by us and linked to our HOD model calculation software.

4. Results

Using Equation (8) in Section 3.1, we calculate the ACF of galaxies at $0.6 < z < 1.4$ and $1.4 < z < 2.6$, respectively. Also,

---

[16] http://helios.fmi.fi/~lainema/mcmcf90/

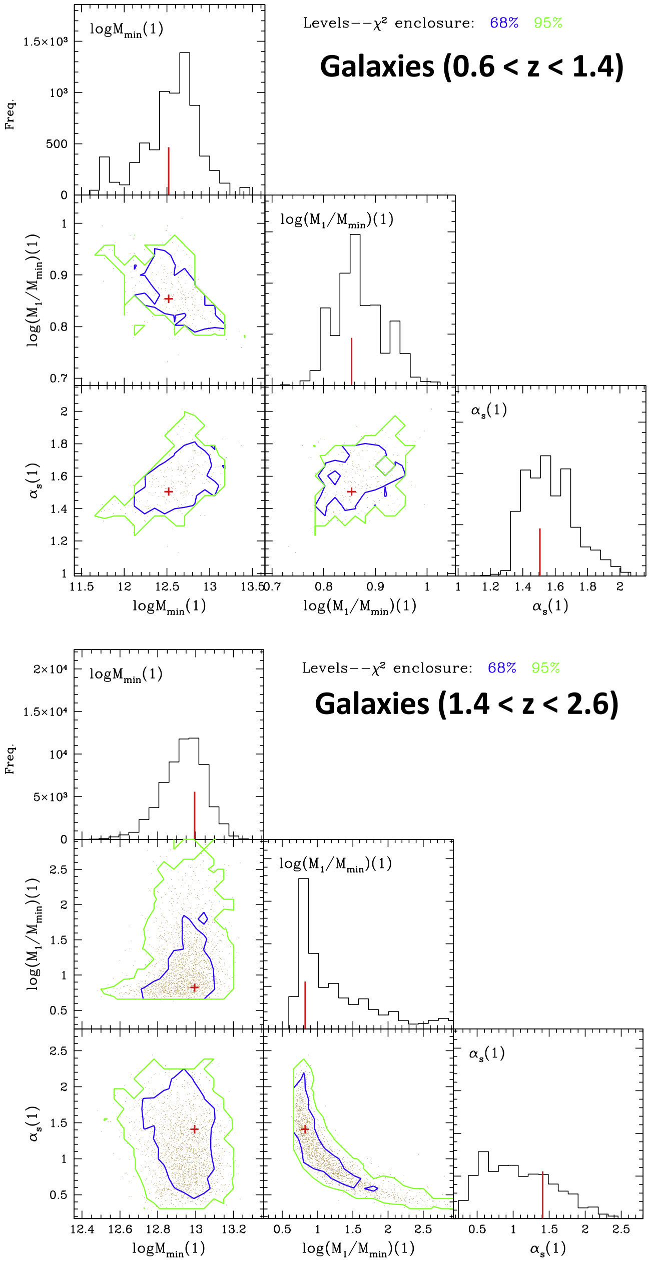

Figure 5. Upper: the confidence contours of the best-fit HOD model for galaxies at $0.6 < z < 1.4$. These confidence contours are estimated from the joint fit to the galaxy ACF and the galaxy–AGN CCF for the $0.6 < z < 1.4$ sample. The red crosses in each off-diagonal panel denote the best-fit values in the corresponding two parameters, while the red vertical lines in each diagonal panel are the best-fit values of the corresponding single parameter. The blue and green contours are drawn at the χ^2 levels below which 68% and 95% of the MCMC chain points fall, respectively. The small brown dots represent the MCMC points. Each diagonal panel shows a histogram of the distributions of the MCMC points in a single parameter space, as labeled. Each parameter name label is accompanied by a "(1)," to indicate that it is for the galaxy sample. Lower: same as the upper panel but for the $1.4 < z < 2.6$ galaxy sample.

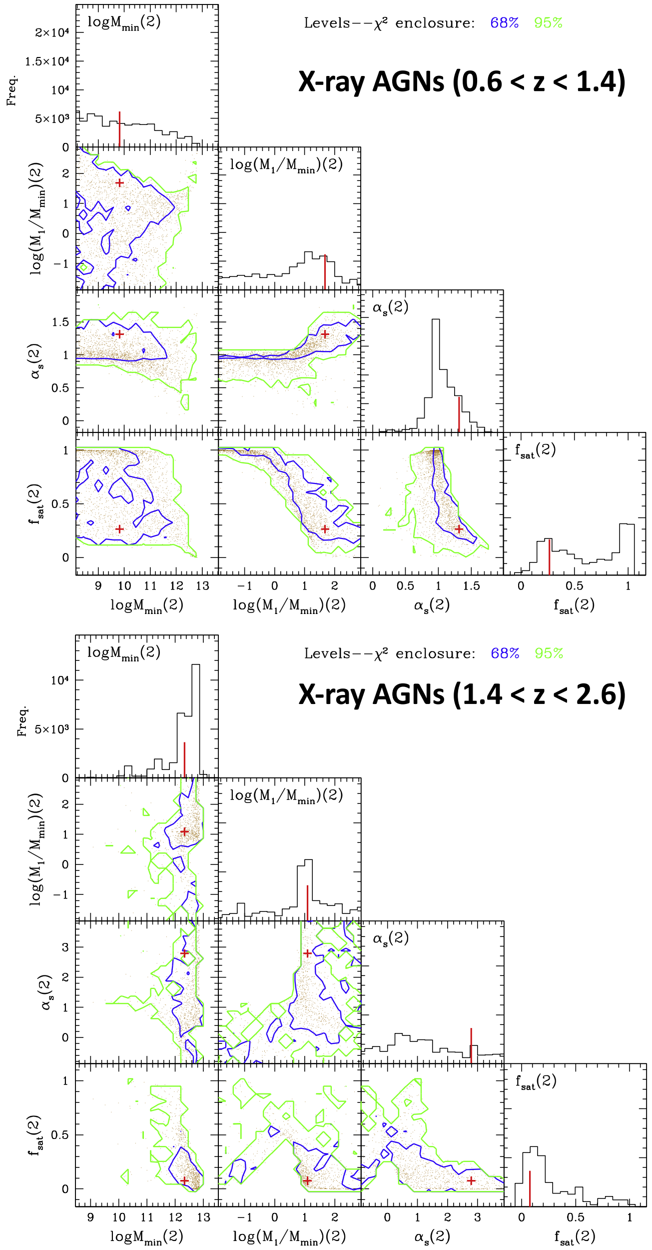

Figure 6. Upper: the confidence contours of the best-fit HOD model for the $0.6 < z < 1.4$ X-ray-selected AGN sample. These confidence contours are obtained from the joint fit to the ACF and galaxy–AGN CCF. The meanings of the symbols and line colors are the same as in Figure 5. The attachment "(2)" in each parameter name label indicates that it is for the X-ray-selected AGN sample. Lower: same as the upper panel but for the $1.4 < z < 2.6$ X-ray-selected AGN sample.

using Equation (10) in Section 3.2, we calculate the CCF of galaxies and AGNs at $0.6 < z < 1.4$ and $1.4 < z < 2.6$, respectively. The jackknife resampling technique calculates the errors of the ACF and CCF. Figure 4 shows our ACF/CCF measurements with the best-fit models and fit residuals. The measurements of the $r_{\rm p} > 10$ bin are plotted for reference, but not included in the fitting process, because this bin corresponds to angular scales comparable to or larger than those of the jackknife zones. Due to the large error and low measured value of the smallest angular bin of the $1.4 < z < 2.6$ CCF, this bin is not included in the fit either. The corresponding angular scale of this bin is comparable to the Chandra PSF at larger off-axis angles, and the blending of multiple sources is a likely cause of its low value.

Then we obtain constraints on the AGN HOD parameters, such as $M_{\rm min}$ and $\alpha_{\rm s}$. Using these two parameters, we can

Table 3
The HOD Parameters

Sample	Redshift Range	$\log M_{\rm min}$ $(h^{-1}\,M_\odot)$	$\log\langle M_{\rm DMH}\rangle$ $(h^{-1}\,M_\odot)$	α_s	Linear Bias	$\log M_{\rm typ}$ $(h^{-1}\,M_\odot)$	$\log(M_1/M_{\rm min})$
Galaxy	$0.6 < z < 1.4$	12.89 (12.31; 12.95)	12.85 (12.78; 12.86)	1.58 (1.42; 1.74)	1.50 (1.33; 1.52)	12.42 (12.16; 12.44)	0.82 (0.81; 0.93)
Galaxy	$1.4 < z < 2.6$	12.99 (12.83; 13.04)	12.45 (12.37; 12.46)	1.41 (0.57; 1.62)	2.03 (1.92; 2.06)	12.18 (12.06; 12.20)	0.82 (0.78; 1.03)
AGN	$0.6 < z < 1.4$	9.82 (8.54; 11.37)	12.84 (12.72; 12.92)	1.31 (0.90; 1.29)	1.16 (1.16; 1.31)	11.82 (11.82; 12.12)	1.69 (−0.93;1.82)
AGN	$1.4 < z < 2.6$	12.34 (11.67; 12.78)	13.01 (12.61; 13.13)	2.79 (− 0.13; 2.77)	2.95 (2.30; 3.55)	12.80 (12.38; 13.06)	1.09 (−0.45;1.99)

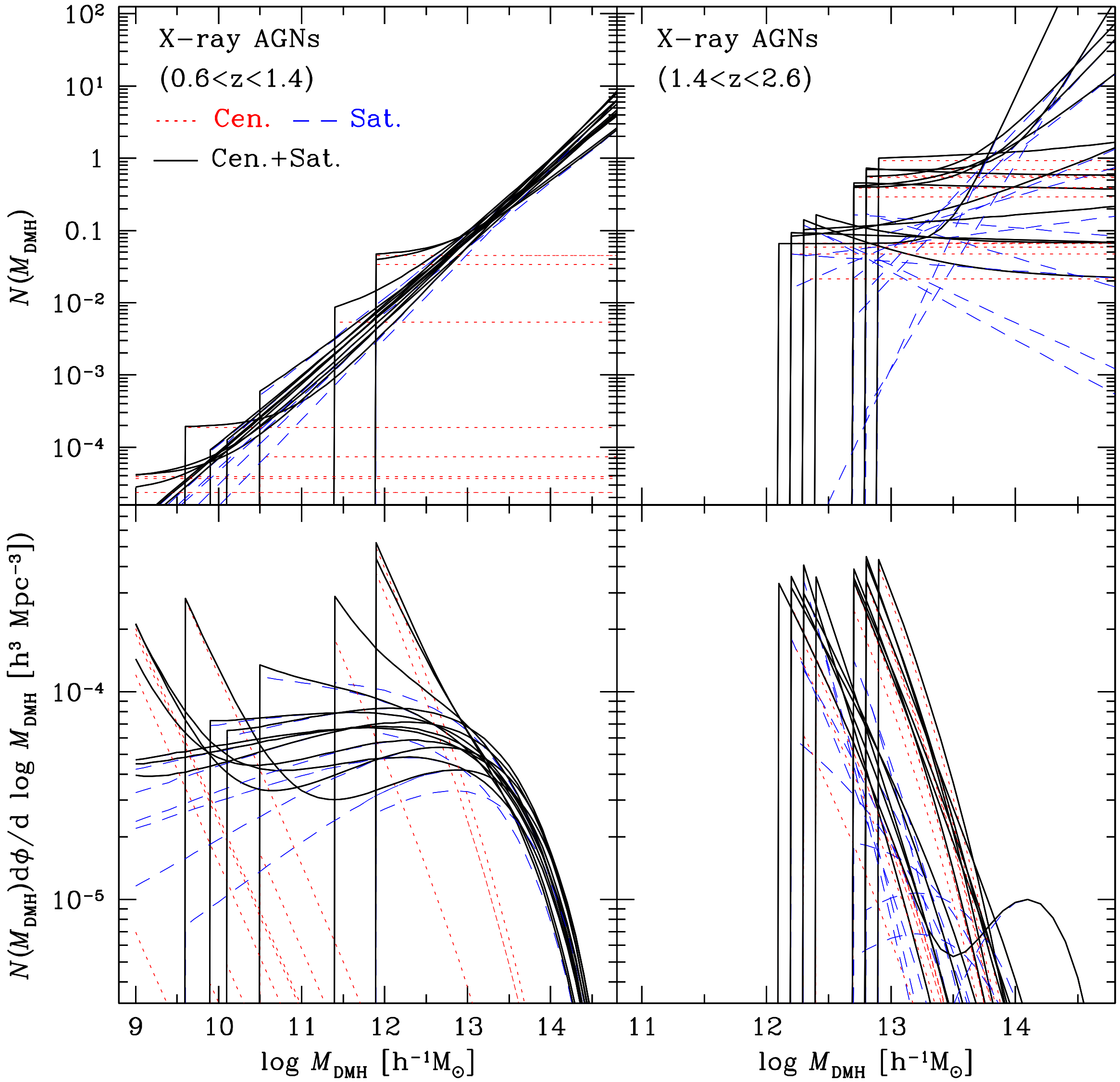

Figure 7. HODs of accepted models for the X-ray-selected AGN sample. The upper left and right panels show the HODs for the $0.6 < z < 1.4$ and $1.4 < z < 2.6$ AGN samples, respectively. In each panel, the red dotted, blue dashed, and black solid lines show acceptable randomly selected models for central ($\langle N_{\rm A,c}\rangle$), satellite ($\langle N_{\rm A,s}\rangle$), and the central+satellite HODs. The models are selected from the chain points of our MCMC run that are among the 68% smallest χ^2 of all chain points. The lower panels show the central+satellite HODs multiplied by the DMH mass function.

calculate the mean DMH mass occupied by the X-ray AGN sample:

$$\langle M_{\rm DMH}\rangle = \frac{\int M_{\rm DMH}\langle N_{\rm A}\rangle(M_{\rm DMH})\phi(M_{\rm DMH})dM_{\rm DMH}}{\int\langle N_{\rm A}\rangle(M_{\rm DMH})\phi(M_{\rm DMH})dM_{\rm DMH}}, \quad (19)$$

while the effective linear bias parameters of galaxies and AGNs, respectively, are calculated as follows:

$$b_{\rm G} = \frac{\int b_{\rm DMH}(M_{\rm DMH})\langle N_{\rm G}\rangle(M_{\rm DMH})\phi(M_{\rm DMH})dM_{\rm DMH}}{\int\langle N_{\rm G}\rangle(M_{\rm DMH})\phi(M_{\rm DMH})dM_{\rm DMH}} \quad (20)$$

$$b_{\rm A} = \frac{\int b_{\rm DMH}(M_{\rm DMH})\langle N_{\rm A}\rangle(M_{\rm DMH})\phi(M_{\rm DMH})dM_{\rm DMH}}{\int\langle N_{\rm A}\rangle(M_{\rm DMH})\phi(M_{\rm DMH})dM_{\rm DMH}}. \quad (21)$$

The confidence contours of the HOD model parameters for galaxies at $0.6 < z < 1.4$ and $1.4 < z < 2.6$ are shown in off-diagonal panels in Figure 5 in two-dimensional projected parameter spaces. The 68% and 95% confidence contours are drawn along equal χ^2 values. For each panel in each two-parameter grid bin, we find many MCMC points, which have different values of other parameters and, accordingly, different χ^2 values. We pick the smallest χ^2 value to represent this two-dimensional parameter bin and use these χ^2 values for contouring. The two χ^2 contour levels are determined such that 68% and 95% of all the MCMC chain points fall below these χ^2 levels, respectively. We also plot histograms of the MCMC points in single parameters in the diagonal panels. In the same way, the confidence contours and histograms of the HOD models are shown for the $0.6 < z < 1.4$ and $1.4 < z < 2.6$ X-ray-selected AGN samples in Figure 6. Table 3 summarizes the estimated HOD parameters, the derived linear bias parameter, and the typical DMH mass ($M_{\rm typ}$). Here, $M_{\rm typ}$ is defined by $b_{\rm DMH}(M_{\rm typ}) = b_{\rm lin}$, where $b_{\rm lin}$ is the observed linear bias parameter for the sample. In

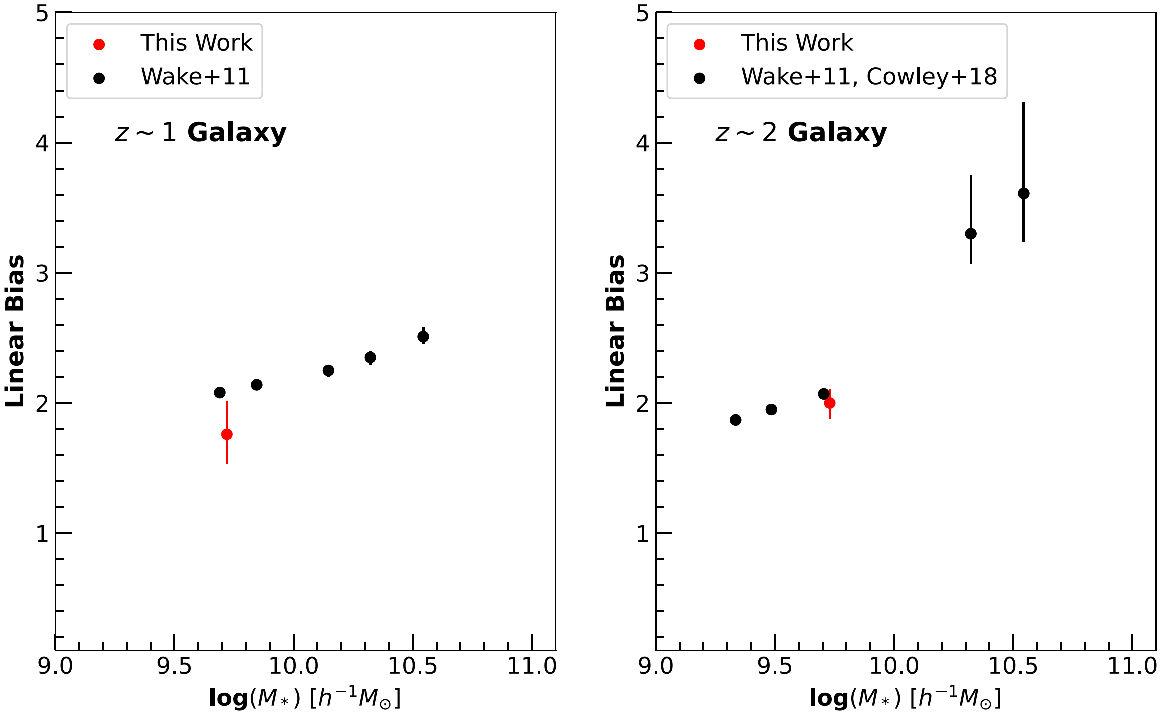

Figure 8. Left: $z \sim 1$ galaxy linear bias as a function of stellar mass. The red and black points represent our results and results in the literature (D. A. Wake et al. 2011). The error bars of our results are at the 68% confidence level (between the 16% and 84% percentiles from the corresponding MCMC chains) for one interesting parameter. Right: the same as the left panel but for $z \sim 2$ galaxy linear bias. The red and black points represent our results and results in the literature (D. A. Wake et al. 2011; W. I. Cowley et al. 2018).

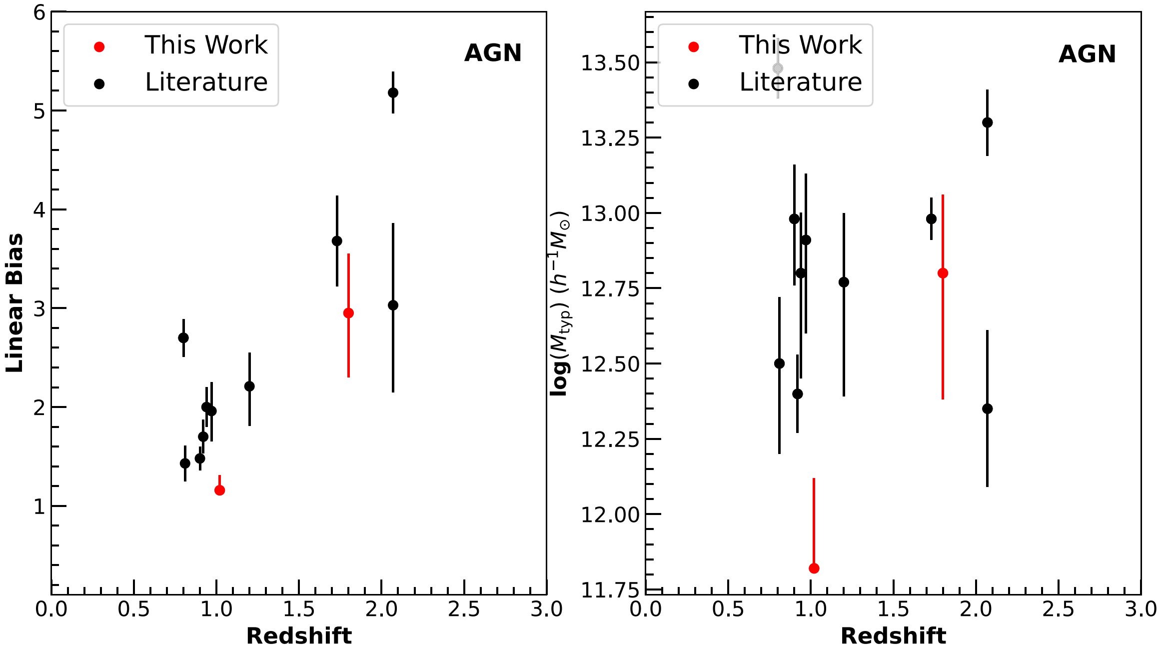

Figure 9. Left: redshift evolution of X-ray-selected AGN bias. The red and black points represent our results and results in literature ordered according to redshift (Y. Yang et al. 2006; A. L. Coil et al. 2009; R. Gilli et al. 2009; V. Allevato et al. 2011; G. Mountrichas et al. 2013, 2016; M. Plionis et al. 2018; A. Viitanen et al. 2019). The error bars of our results are at the 68% confidence level (between the 16% and 84% percentiles from the corresponding MCMC chains) for one interesting parameter. Right: redshift evolution of $\log M_{\rm typ}$ for X-ray-selected AGNs. The red and black points represent our results and results in the literature ordered according to redshift (Y. Yang et al. 2006; A. L. Coil et al. 2009; R. Gilli et al. 2009; V. Allevato et al. 2011; G. Mountrichas et al. 2013, 2016; M. Plionis et al. 2018; A. Viitanen et al. 2019). The error bars of our results are at the 68% confidence level (between the 16% and 84% percentiles from the corresponding MCMC chains) for one interesting parameter.

Table 3, the best-fit value of each parameter is from the minimum χ^2 model, and the 68% confidence range is shown in parentheses, which is derived from the marginalized distributions of the MCMC chain. In rare cases, the probability distribution is skewed and the nominal value can be slightly outside the 68% confidence range.

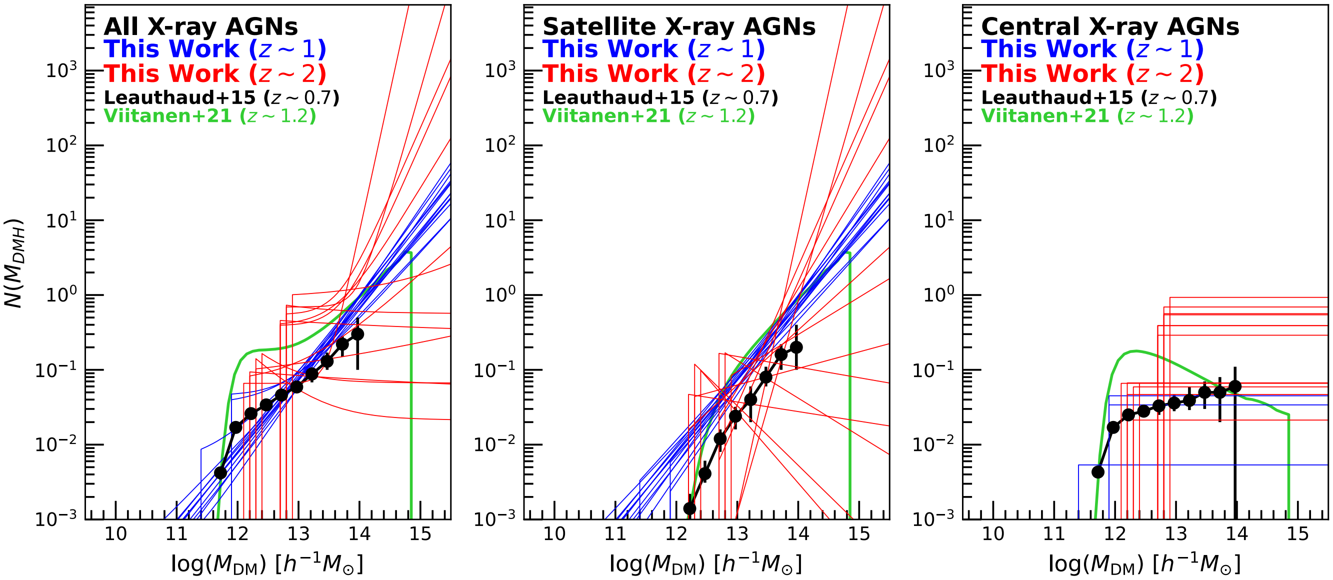

Figure 10. Comparison between the HODs of X-ray-selected AGNs at $z\sim1$ and $z\sim2$. In each panel, the blue and red solid lines show the 68% confidence ranges of the central ($\langle N_{\rm A,c}\rangle$), satellite ($\langle N_{\rm A,s}\rangle$), and central+satellite HODs. The blue and red lines show the central+satellite HODs at $z\sim1$ and $z\sim2$, respectively. The black circles show the HOD of X-ray-selected AGNs at $z\sim0.7$, as derived by A. Leauthaud et al. (2015). The green lines show the HOD of mock AGNs at $z\sim1.2$, as derived by A. Viitanen et al. (2021).

Figure 7 (upper panels) shows random selections of acceptable AGN HOD models for the central, satellite components, and the total, where we consider models with the smallest 68% χ^2 in the MCMC chain acceptable. In the figure labels and text, we express various HODs as "$N(M_{\rm DMH})$" generically. The $N(M_{\rm DMH})$ values have been normalized to have the effective space density of the sample, which is the number of AGNs divided by the total comoving volume in the field over the redshift range (see Table 2). About half of the initially accepted $z\sim2$ AGN central HOD curves showed $N_{\rm A,c}>1$ (or $f_{\rm A}>1$) upon the normalization, which is unphysical. These have been excluded from the chain, and the 68% confidence ranges are recalculated accordingly. Table 3 (bottom row), Figure 6 (bottom row), and Figure 7 (right panels) show the results of the chain after the exclusion. In the lower panels, we also show $N(M_{\rm DMH})$ multiplied by the halo mass function. For the $z\sim1$ sample, the fraction of initially accepted HOD chain points that give $N_{\rm A,c}>1$ is less than 1% and therefore neglected.

5. Discussion

5.1. The Bias and DMH Mass

To investigate whether the calculated galaxy bias aligns with previous measurements, we compare the galaxy bias and $\log M_{\rm typ}$ of galaxies at approximately $z=1$ and $z=2$ with the literature (D. A. Wake et al. 2011; W. I. Cowley et al. 2018). The results of this comparison are illustrated in Figure 8. At around $z=1$, we find a galaxy bias of 1.50 (1.33; 1.52). At $z\sim2$, our analysis yields a galaxy bias of 2.03 (1.92; 2.06).

Similar findings were reported by D. A. Wake et al. (2011), based on a galaxy sample from the NOAO Extremely Wide-Field Infrared Imager Medium-Band Survey. Their analysis resulted in a galaxy bias of $2.08^{+0.04}_{-0.03}$ at $z\approx1$. Furthermore, W. I. Cowley et al. (2018) derived a galaxy bias of 2.07 ± 0.04 at $z\approx2$. Consequently, our study confirms the general consistency between the galaxy bias at $z\sim1$–2 with previous measurements.

Figure 9 shows the evolution of the AGN bias parameter and the associated $M_{\rm typ}$ from this work and from the literature. From this work, the AGN linear bias $b_{\rm A}$ and $M_{\rm typ}$ are significantly larger at $z\sim2$ than at $z\sim1$. Since the COSMOS Legacy sample is essentially flux-limited, the $z\sim2$ sample contains more luminous AGNs than the $z\sim1$ sample. To trace the redshift evolution of the halo masses of AGNs on the same ground, we need to combine the results from different surveys. A caveat is that each sample from the literature covers different X-ray-selected AGN selection criteria in terms of energy bands, luminosities, and the redshift range.

In order to assess the consistency of the calculated AGN bias with previous measurements, we conduct a comparison of the AGN bias and the logarithm of $M_{\rm typ}$ for X-ray-selected AGNs at approximately $z\sim1$ and $z\sim2$, with reference to a study in the literature (A. L. Coil et al. 2009). At around $z\sim1$, we determine an inferred AGN bias of 1.16 (1.16; 1.31), which corresponds to a DMH mass of $\log(M_{\rm typ}/M_\odot)=11.82$ (11.82; 12.12). In comparison, the AGN bias and $\log(M_{\rm typ})$ values for X-ray-selected AGNs at $z\sim1$, as reported in A. L. Coil et al. (2009), stand at 1.48 ± 0.12 and 12.98 (12.76; 13.16), respectively. For X-ray-selected AGNs at $z\sim2$, our calculations yielded an AGN bias of 2.95 (2.30; 3.55) and a $\log(M_{\rm typ}/M_\odot)$ of 12.80(12.38; 13.06). In contrast, V. Allevato et al. (2011) investigated the AGN bias at $z\sim2$ using Equation (16) in V. Allevato et al. (2011), and they estimated that the AGN bias at $z\sim2$ is 5.18 ± 0.21, which corresponds to $\log(M_{\rm typ}/M_\odot)$ of 13.30 ± 0.11. We note that the typical DMH mass derived from the large-scale bias may not reflect the true distribution of the AGN host halo masses. This is especially the case if the underlying AGN host halo mass distribution spans a range of halo masses in different large-scale environments. For example, A. Leauthaud et al. (2015) found a skewed distribution of AGN host DMH masses in COSMOS, where the typical DMH masses reported earlier resided between their median (lower) and mean (higher) values. Also, using DMHs from large N-body simulations and empirically motivated AGN models, J. Aird & A. L. Coil

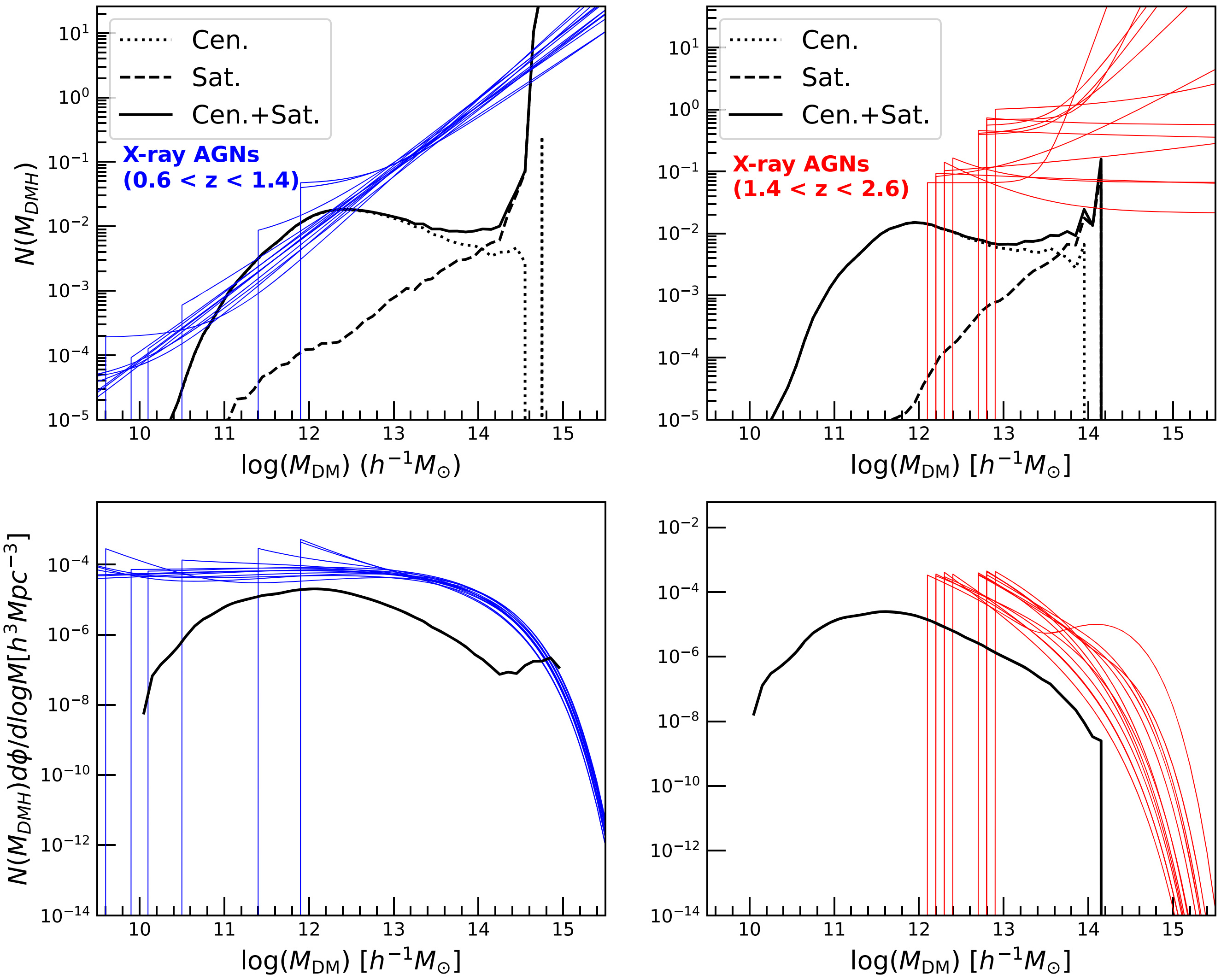

Figure 11. Comparison between the HOD of our results and theoretical predictions from the Uchuu-nu2GC catalogs. In each panel, the dotted, dashed, and solid lines show the HODs of central ($\langle N_{\rm A,c}\rangle$), satellite ($\langle N_{\rm A,s}\rangle$), and central+satellite HODs. The blue and red lines show the central+satellite HODs at $z \sim 1$ and $z \sim 2$, respectively.

(2021) found that the true bias calculated directly from the DMHs is systematically lower than the observationally measured one.

5.2. The HOD of X-Ray-selected AGNs at $z \sim 1$ and $z \sim 2$

To investigate the redshift-dependent behavior of the HODs of X-ray-selected AGNs in detail, we present the HODs of X-ray-selected AGNs at $z \sim 1$ and $z \sim 2$ in Figure 10. The blue lines represent the HODs of X-ray-selected AGNs at $z \sim 1$. Similarly, the red lines show the HODs of X-ray-selected AGNs at $z \sim 2$.

Under this form of the HOD model (Equations (15) and (16)), there are two peaks in the distribution of $f_{\rm sat}$ for $z \sim 1$ AGNs, where all or mostly central models are highly unlikely, with only 1.4% of the points in the MCMC chain giving $f_{\rm sat} < 0.05$. At $z \sim 2$, the HOD analysis suggests a small fraction of satellites, with all/mostly central models being highly unlikely, with only 1.5% of the MCMC chain points giving $f_{\rm sat} > 0.95$ (see the histograms in the lower right corners in each row of Figure 6.) At these redshifts, the halo mass function drops rapidly at group-/cluster-sized halos, thus there are practically no $z \sim 2$ rich groups/clusters. Therefore, we focus the discussion on $\log M_{\rm DMH} < 13$.

A. Leauthaud et al. (2015) measured the X-ray-selected AGN HOD at $z \sim 0.7$ in COSMOS using weak gravitational lensing. A. Viitanen et al. (2021) also derived HODs of mock AGNs at $z \sim 1.2$ with different Q values. They define $Q = U_{\rm sat}/U_{\rm cen}$, where $U_{\rm sat}$ and $U_{\rm cen}$ are the duty cycles for the satellite and central BHs, respectively. Since the HOD of mock AGNs at $z \sim 1.2$ with $Q = 1$ agrees with that of other studies (e.g., J. Aird & A. L. Coil 2021), we show it as a representative example of the HODs derived by A. Viitanen et al. (2021) in Figure 10. The HOD of our results at $z \sim 1$ is generally consistent with that of A. Leauthaud et al. (2015) and A. Viitanen et al. (2021).

We perform a comparison between our findings and the theoretical results presented by T. Oogi et al. (2020). T. Oogi et al. (2020) predicted the X-ray-selected AGN bias using semi-analytic modeling of AGNs, verifying that their results are broadly consistent with observational findings. Our results are also in good agreement with the predictions made by T. Oogi et al. (2020). We compare our HOD results with theoretical predictions. To facilitate this comparison, we have constructed

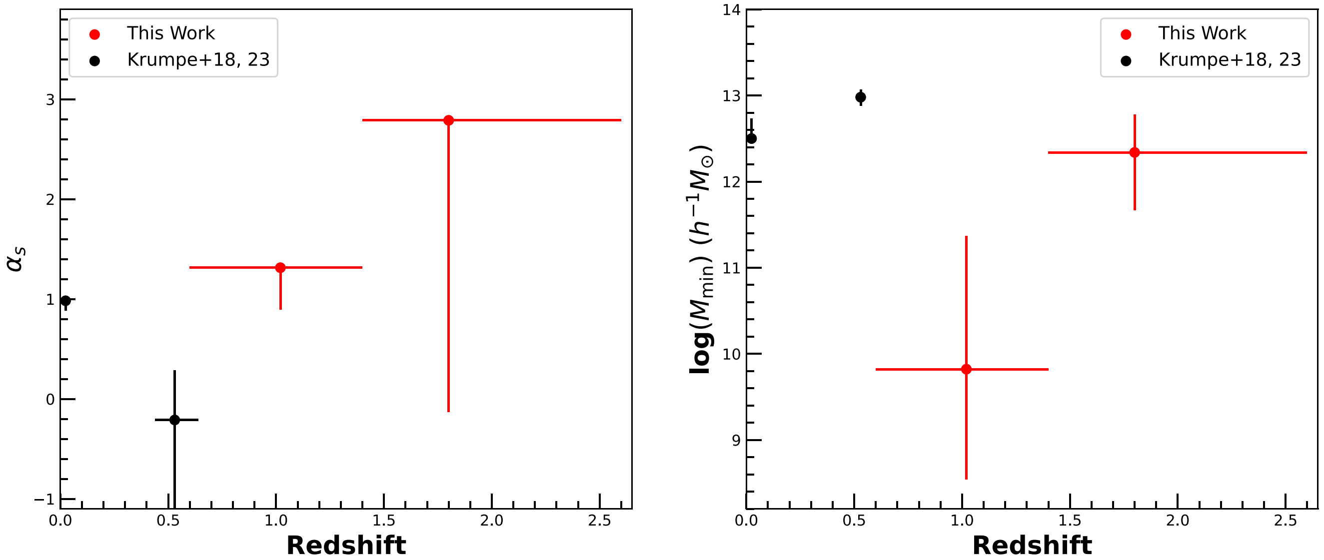

Figure 12. Redshift evolution of α_s (satellite slope) and $\log(M_{\rm min}/M_\odot)$. The red and black points represent our results and the results in the literature (M. Krumpe et al. 2018, 2023). The error bars of our results are at the 68% confidence level (between the 16% and 84% percentiles from the corresponding MCMC chains) for one interesting parameter.

HODs for theoretical predictions at $z \sim 2$. Since the $z \sim 2$ HOD itself is not presented by T. Oogi et al. (2020), we generated the HODs at $z \sim 1$ and $z \sim 2$ using the Ucchu + nu2GC galaxies and AGN catalog (T. Oogi et al. 2023). This catalog is generated by utilizing the Uchuu simulation, which is a 2.1 trillion N-body simulation that uses Planck cosmology (T. Ishiyama et al. 2021). The comparison between our observational results and the theoretical predictions is shown in Figure 11. At $z \sim 1$, our observational data align remarkably well with the theoretical predictions, falling within the margins of error.

Next, we show the redshift evolution of α_s in the left panel of Figure 12. T. Miyaji et al. (2011) and M. Krumpe et al. (2018, 2023) conducted HOD modeling of X-ray-selected AGNs at $z < 1$ and reported $0 \lesssim \alpha_s \lesssim 1$. In contrast, our analysis estimates α_s at $z \sim 1$–2, revealing a trend of increasing α_s with redshift, with α_s at $z \sim 1$–2 being greater than 0. As M. Krumpe et al. (2023) mentioned, $\alpha_s > 0$ indicates that the number of AGNs in satellite galaxies increases with $M_{\rm DMH}$. Conversely, $\alpha_s < 0$ suggests that AGNs in satellite galaxies are more commonly found in lower-mass halos and are infrequent in high-mass halos. Therefore, the results of this study suggest that the number of AGNs in satellite galaxies gradually increases with $M_{\rm DMH}$ up to $z = 2$. We also show the redshift evolution of $\log(M_{\rm min}/M_\odot)$ in the right panel of Figure 12. We find that $\log(M_{\rm min}/M_\odot)$ of the X-ray-selected AGNs at $z < 1$ is ∼12.5–13.0, but that of X-ray-selected AGNs at $z \sim 1$–2 is <12.5.

6. Summary

We have calculated the ACF of galaxies and the CCF of galaxies and X-ray-selected AGNs at $0.6 < z < 2.6$ in the COSMOS field, to estimate the HODs of X-ray-selected AGNs up to $z \sim 2$. The main results of our work are summarized below.

1. We have performed the HOD modeling of X-ray-selected AGNs by utilizing the ACF of galaxies and the CCF of galaxies and AGNs at $z \sim 1$–2.
2. We have estimated AGN bias values of $b = 1.16$ (1.16; 1.31) and $b = 2.95$ (2.30; 3.55), respectively. These values correspond to typical host DMH masses of $\log(M_{\rm typ}/M_\odot) = 11.82$ (11.82; 12.12) and $\log(M_{\rm typ}/M_\odot) = 12.80$ (12.38; 13.06), respectively.
3. We have found a significant satellite AGN population at $z \sim 1$ all over the DMH mass range occupied by AGNs. While $z \sim 2$ AGNs in our sample are associated with higher-mass DMHs, the satellite fraction is smaller.
4. The HOD analysis suggests a marginal tendency of increasing α_s with redshift, but larger samples are needed to confirm this with sufficient statistical significance.
5. We have found that the best-fit values of α_s in both redshift bins are greater than 0, suggesting the tendency of an increasing satellite AGN number with $M_{\rm DMH}$.

Acknowledgments

We thank Mara Salvato for providing us with the PDzs for the X-ray source counterparts of the Chandra-COSMOS Legacy Survey. We thank Instituto de Astrofisica de Andalucia (IAA-CSIC), Centro de Supercomputacion de Galicia (CESGA), and the Spanish academic and research network (RedIRIS) in Spain for hosting Uchuu DR1, DR2 and DR3 at the skies and universes site for cosmological simulations. The Uchuu simulations were carried out on the Aterui II supercomputer at the Center for Computational Astrophysics, CfCA, National Astronomical Observatory of Japan and on the K computer at the RIKEN Advanced Institute for Computational Science. The Uchuu data release efforts have been made using the skun@IAA_RedIRIS and skun6@IAA computer facilities managed by the IAA-CSIC in Spain (MICINN EU-Feder grant EQC2018-004366-P). Data analysis was in part carried out on the Multiwavelength Data Analysis System operated by the Astronomy Data Center (ADC), National Astronomical Observatory of Japan.

This work is supported by UNAM-DGAPA PAPIIT No. IN111319, IN114423, and CONACyT grant Cientìfica Básica 252531 (T.M.). This work is also supported by JSPS

KAKENHI grant Nos. 23K03465 (H.I.), 22H01266 (Y.T.), 21H05449, and 23K03460 (T.O.). T.M. thanks JSPS for financial support under the "Invitational Fellowship for Research in Japan (L24523)" program and Yoshihiro Ueda and Kyoto University for their hospitality during his sabbatical stay.

Appendix
Covariance Matrix

The errors in different bins of the CFs are mutually correlated and the χ^2 in the presence of the correlated errors can be treated with the covariance matrix (Equation (11)) constructed from jackknife resamplings with Equation (18). For accurate measurements of the covariance matrix, a large number of jackknife zones that are statistically independent from one another would be ideal. However, the number of jackknife zones is limited by the size of each zone, which should be larger than the largest r_p scale to be measured, so that each zone is as statistically independent as possible. Strictly speaking, when there are pairs across different zones, the statistical independence is not met to some degree. This is a fundamental limitation of using this method.

In the case of a small field such as ours, we can divide the field into only a small number of jackknife zones (16, in our case) and some off-diagonal regions of the covariance matrix become noise-dominated (e.g., Y. Herrero Alonso et al. 2023). This can cause the model with the minimum correlated χ^2 to significantly deviate from the data. To avoid this problem, we clean the covariance matrix by ignoring some off-diagonal parts. We have tried the following covariance matrices: (i) uncorrelated χ^2 (all off-diagonal elements are 0); (ii) full covariance matrix, keeping all off-diagonal elements, including those between different r_p bins within each of the galaxy ACF and galaxy–AGN CCF as well as elements across them; (iii) the off-diagonal elements across the ACF and CCF are set to 0, while keeping those within each; and (iv) only off-diagonal elements within the CCF are kept. Figure 13 (left) shows the ratios of the actual measurements with the models that give minimum χ^2 using covariance matrices (i)–(iv). Naturally, using uncorrelated χ^2 (i) gives the best apparent fits to the data. However, under the existence of the correlations among the data errors, the parameter errors/confidence ranges obtained using (i) may well be misestimated. The correct method is to use the full covariance matrix (ii), if it is accurate enough. However, we observe that the best-fit model using this option significantly underestimates the $0.6 < z < 1.4$ ACF at $r_p \gtrsim 1h^{-1}$[Mpc] and the $1.4 < z < 2.6$ CCF at $r_p \gtrsim 2h^{-1}$[Mpc]. Similar deviations remain for the $0.6 < z < 1.4$ ACF, even if the off-diagonal elements across the ACF/CCF are set to 0. Yet another option is to keep the off-diagonal elements within the CCF, while setting the others to 0 (iv). As seen in Figure 13 (left), the best-fit models with this option are almost identical to those with option (i) for both redshift ranges. Figure 13 (right) compares the AGN HOD parameters that give minimum χ^2 and confidence ranges estimated by the marginal distributions of MCMC chain points for options (i)–(iv). This panel shows that option (i) (uncorrelated χ^2) gives distinctively different errors for some parameters, while those from other options give approximately the same. Option (iv) (only off-diagonal elements within the CCF are kept) does not show significant residuals of the fit at the same time, giving errors similar to those from option (ii) (full covariance matrix). Thus, in this work, we choose to use option (iv) for further analysis.

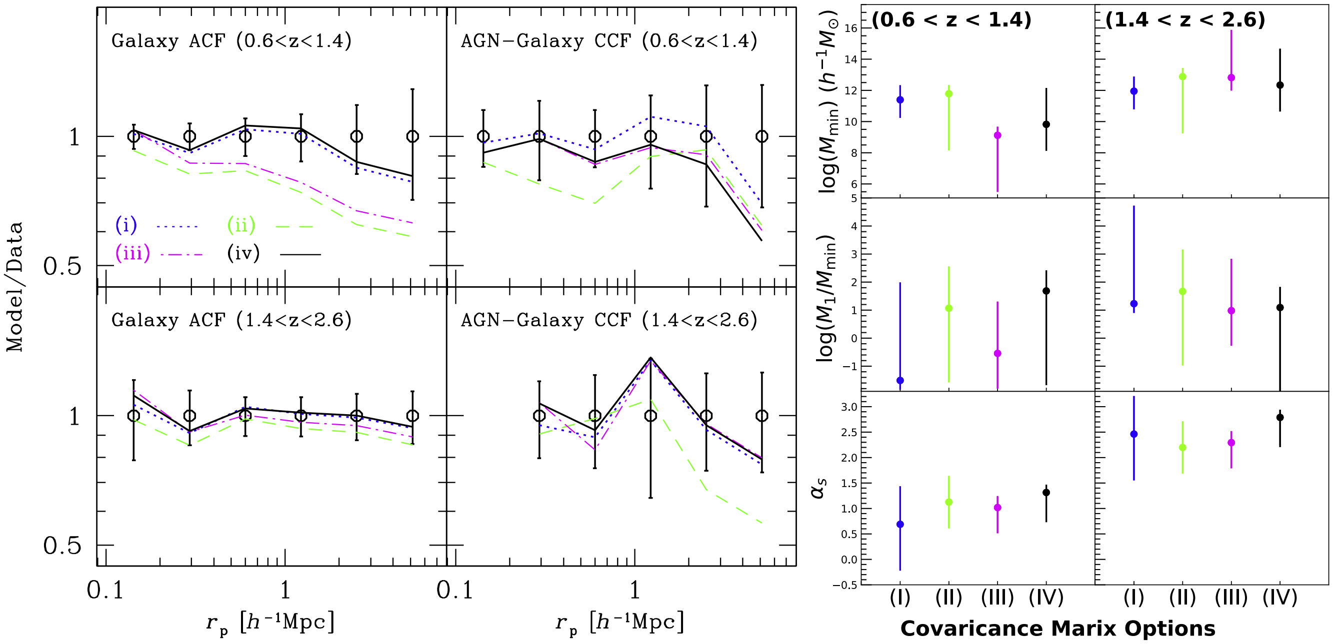

Figure 13. Left: ratios of the $w_p(r_p)$ models giving minimum χ^2 with different covariance matrix options to the measured values. The circles with 1σ error bars represent the measurements used for the fits. The blue dotted, green dashed, magenta dotted–dashed, and black solid lines are the models divided by the measured values corresponding to the covariance matrix options (i)–(iv) (see the text). Right: minimum χ^2 parameter values for the AGN HODs and associated 68% errors for the covariance matrix options (i)–(iv).

ORCID iDs

Hiroyuki Ikeda https://orcid.org/0000-0002-1207-1979
Takamitsu Miyaji https://orcid.org/0000-0002-7562-485X
Yoshiki Toba https://orcid.org/0000-0002-3531-7863
Héctor Aceves https://orcid.org/0000-0002-7348-8815
Stefano Marchesi https://orcid.org/0000-0001-5544-0749
Viola Allevato https://orcid.org/0000-0001-7232-5152
Akke Viitanen https://orcid.org/0000-0001-9383-786X
Francesca Civano https://orcid.org/0000-0002-2115-1137

References

Adelberger, K. L., & Steidel, C. C. 2005, ApJL, 627, L1
Adelberger, K. L., Steidel, C. C., Shapley, A. E., & Pettini, M. 2003, ApJ, 584, 45
Aird, J., & Coil, A. L. 2021, MNRAS, 502, 5962
Aird, J., Coil, A. L., Georgakakis, A., et al. 2015, MNRAS, 451, 1892
Akiyama, M., He, W., Ikeda, H., et al. 2018, PASJ, 70, S34
Allevato, V., Civano, F., Finoguenov, A., et al. 2016, ApJ, 832, 70
Allevato, V., Finoguenov, A., Cappelluti, N., et al. 2011, ApJ, 736, 99
Allevato, V., Finoguenov, A., Civano, F., et al. 2014, ApJ, 796, 4
Allevato, V., Viitanen, A., Finoguenov, A., et al. 2019, A&A, 632, A88
Ananna, T. T., Treister, E., Urry, C. M., et al. 2019, ApJ, 871, 240
Bradshaw, E. J., Almaini, O., Hartley, W. G., et al. 2011, MNRAS, 415, 2626
Civano, F., Marchesi, S., Comastri, A., et al. 2016, ApJ, 819, 62
Coil, A. L., Georgakakis, A., Newman, J. A., et al. 2009, ApJ, 701, 1484
Cooray, A., & Sheth, R. 2002, PhR, 372, 1
Cowley, W. I., Caputi, K. I., Deshmukh, S., et al. 2018, ApJ, 853, 69
Croom, S. M., Richards, G. T., Shanks, T., et al. 2009, MNRAS, 399, 1755
Fotopoulou, S., Buchner, J., Georgantopoulos, I., et al. 2016, A&A, 587, A142
Francke, H., Gawiser, E., Lira, P., et al. 2008, ApJL, 673, L13
Garcìa-Vergara, C., Hennawi, J. F., Barrientos, L. F., & Arrigoni Battaia, F. 2019, ApJ, 886, 79
Garcìa-Vergara, C., Hennawi, J. F., Barrientos, L. F., & Rix, H.-W. 2017, ApJ, 848, 7
Gilli, R., Zamorani, G., Miyaji, T., et al. 2009, A&A, 494, 33
Hasinger, G., Miyaji, T., & Schmidt, M. 2005, A&A, 441, 417
He, W., Akiyama, M., Bosch, J., et al. 2018, PASJ, 70, S33
Herrero Alonso, Y., Miyaji, T., Wisotzki, L., et al. 2023, A&A, 671, A5
Ikeda, H., Nagao, T., Matsuoka, K., et al. 2011, ApJL, 728, L25
Ikeda, H., Nagao, T., Matsuoka, K., et al. 2012, ApJ, 756, 160
Ikeda, H., Nagao, T., Taniguchi, Y., et al. 2015, ApJ, 809, 138
Ishiyama, T., Prada, F., Klypin, A. A., et al. 2021, MNRAS, 506, 4210
Kashikawa, N., Ishizaki, Y., Willott, C. J., et al. 2015, ApJ, 798, 28
Kashikawa, N., Kitayama, T., Doi, M., et al. 2007, ApJ, 663, 765
Koutoulidis, L., Plionis, M., Georgantopoulos, I., & Fanidakis, N. 2013, MNRAS, 428, 1382
Krishnan, C., Almaini, O., Hatch, N. A., et al. 2020, MNRAS, 494, 1693
Krumpe, M., Miyaji, T., Coil, A. L., & Aceves, H. 2012, ApJ, 746, 1
Krumpe, M., Miyaji, T., Coil, A. L., & Aceves, H. 2018, MNRAS, 474, 1773
Krumpe, M., Miyaji, T., Georgakakis, A., et al. 2023, ApJ, 952, 109
Laigle, C., McCracken, H. J., Ilbert, O., et al. 2016, ApJS, 224, 24
Landy, S. D., & Szalay, A. S. 1993, ApJ, 412, 64
Leauthaud, A., J. Benson, A., Civano, F., et al. 2015, MNRAS, 446, 1874
Marchesi, S., Civano, F., Elvis, M., et al. 2016, ApJ, 817, 34
Matsuoka, Y., Onoue, M., Iwasawa, K., et al. 2023, ApJL, 949, L42
Matsuoka, Y., Strauss, M. A., Kashikawa, N., et al. 2018, ApJ, 869, 150
Miyaji, T., Bravo-Navarro, B. A., Dìaz Tello, J., et al. 2024, A&A, 689, A83
Miyaji, T., Hasinger, G., Salvato, M., et al. 2015, ApJ, 804, 104
Miyaji, T., Krumpe, M., Coil, A. L., & Aceves, H. 2011, ApJ, 726, 83
Miyaji, T., Zamorani, G., Cappelluti, N., et al. 2007, ApJS, 172, 396
Mountrichas, G., Georgakakis, A., Finoguenov, A., et al. 2013, MNRAS, 430, 661
Mountrichas, G., Georgakakis, A., Menzel, M. L., et al. 2016, MNRAS, 457, 4195
Mountrichas, G., Sawangwit, U., Shanks, T., et al. 2009, MNRAS, 394, 2050
Navarro, J. F., Frenk, C. S., & White, S. D. M. 1997, ApJ, 490, 493
Niida, M., Nagao, T., Ikeda, H., et al. 2020, ApJ, 904, 89
Oke, J. B. 1974, ApJS, 27, 21
Oogi, T., Ishiyama, T., Prada, F., et al. 2023, MNRAS, 525, 3879
Oogi, T., Shirakata, H., Nagashima, M., et al. 2020, MNRAS, 497, 1
Peacock, J. A., & Smith, R. E. 2000, MNRAS, 318, 1144
Plionis, M., Koutoulidis, L., Koulouridis, E., et al. 2018, A&A, 620, A17
Ranalli, P., Koulouridis, E., Georgantopoulos, I., et al. 2016, A&A, 590, A80
Salvato, M., Buchner, J., Budavári, T., et al. 2018, MNRAS, 473, 4937
Salvato, M., Ilbert, O., Hasinger, G., et al. 2011, ApJ, 742, 61
Seljak, U. 2000, MNRAS, 318, 203
Shen, Y., McBride, C. K., White, M., et al. 2013, ApJ, 778, 98
Sheth, R. K., Mo, H. J., & Tormen, G. 2001, MNRAS, 323, 1
Shirasaki, Y., Akiyama, M., Toba, Y., He, W., & Goto, T. 2020, PASJ, 72, 60
Starikova, S., Cool, R., Eisenstein, D., et al. 2011, ApJ, 741, 15
Tinker, J. L., Weinberg, D. H., Zheng, Z., & Zehavi, I. 2005, ApJ, 631, 41
Toba, Y., Nagao, T., Kajisawa, M., et al. 2017, ApJ, 835, 36
Ueda, Y., Akiyama, M., Hasinger, G., Miyaji, T., & Watson, M. G. 2014, ApJ, 786, 104
Ueda, Y., Akiyama, M., Ohta, K., & Miyaji, T. 2003, ApJ, 598, 886
Ueda, Y., Watson, M. G., Stewart, I. M., et al. 2008, ApJS, 179, 124
Viitanen, A., Allevato, V., Finoguenov, A., Shankar, F., & Marsden, C. 2021, MNRAS, 507, 6148
Viitanen, A., Allevato, V., Finoguenov, A., et al. 2019, A&A, 629, A14
Wake, D. A., Whitaker, K. E., Labbé, I., et al. 2011, ApJ, 728, 46
Weaver, J. R., Kauffmann, O. B., Ilbert, O., et al. 2022, ApJS, 258, 11
Yang, J., Wang, F., Wu, X.-B., et al. 2016, ApJ, 829, 33
Yang, Y., Mushotzky, R. F., Barger, A. J., & Cowie, L. L. 2006, ApJ, 645, 68
Zheng, Z., Berlind, A. A., Weinberg, D. H., et al. 2005, ApJ, 633, 791
Zheng, Z., Coil, A. L., & Zehavi, I. 2007, ApJ, 667, 760